RESEARCH ARTICLE

CORONAVIRUS

Distinct conformational states of SARS-CoV-2 spike protein

Yongfei Cai[1,2]*, Jun Zhang[1,2]*, Tianshu Xiao[1,2], Hanqin Peng[1], Sarah M. Sterling[3,4], Richard M. Walsh Jr.[3,4], Shaun Rawson[3,4,5], Sophia Rits-Volloch[1], Bing Chen[1,2]†

Intervention strategies are urgently needed to control the severe acute respiratory syndrome coronavirus 2 (SARS-CoV-2) pandemic. The trimeric viral spike (S) protein catalyzes fusion between viral and target cell membranes to initiate infection. Here, we report two cryo–electron microscopy structures derived from a preparation of the full-length S protein, representing its prefusion (2.9-angstrom resolution) and postfusion (3.0-angstrom resolution) conformations, respectively. The spontaneous transition to the postfusion state is independent of target cells. The prefusion trimer has three receptor-binding domains clamped down by a segment adjacent to the fusion peptide. The postfusion structure is strategically decorated by N-linked glycans, suggesting possible protective roles against host immune responses and harsh external conditions. These findings advance our understanding of SARS-CoV-2 entry and may guide the development of vaccines and therapeutics.

The current coronavirus pandemic is having devastating social and economic consequences. Coronaviruses (CoVs) are enveloped, positive-stranded RNA viruses. They include severe acute respiratory syndrome (SARS) and Middle East respiratory syndrome (MERS), both of which have been associated with significant fatalities (*1*–*3*), as well as several endemic common-cold viruses (*4*). With a large number of similar viruses circulating in bats and camels (*5*–*8*), the possibility of additional outbreaks poses major threats to global public health. The current disease, coronavirus disease 2019 (COVID-19), which is caused by a new virus, SARS-CoV-2 (*9*), has created urgent needs for diagnostics, therapeutics and vaccines. Meeting these needs requires a deep understanding of the structure-function relationships of viral proteins and relevant host factors.

For all enveloped viruses, membrane fusion is a key early step for entering host cells and establishing infection (*10*). Although it is an energetically favorable process, membrane fusion has high kinetic barriers when two membranes approach each other, mainly because of repulsive hydration forces (*11*, *12*). For viral membrane fusion, free energy to overcome these kinetic barriers comes from refolding of virus-encoded fusion proteins from a primed, metastable prefusion conformational state to a stable, postfusion state (*13*–*15*). The fusion protein for CoV is its spike (S) protein that decorates the virion surface as an extensive crown (hence, "corona"). The protein also induces neutralizing antibody responses and is therefore an important target for vaccine development (*16*). The S protein is a heavily glycosylated type I membrane protein anchored in the viral membrane. It is first produced as a precursor that trimerizes and is thought to be cleaved by a furin-like protease into two fragments: the receptor-binding fragment S1 and the fusion fragment S2 (Fig. 1A) (*17*). Binding through the receptor-binding domain (RBD) in S1 to a host cell receptor [angiotensin-converting enzyme 2 (ACE2) for both SARS-CoV and SARS-CoV-2] and further proteolytic cleavage at a second site in S2 (the S2' site) by a serine protease, transmembrane serine protease 2 (TMPRSS2) (*18*), or the endosomal cysteine proteases cathepsins B and L (CatB/L) are believed to trigger dissociation of S1 and irreversible refolding of S2 into a postfusion conformation, a trimeric hairpin structure formed by heptad repeat 1 (HR1) and heptad repeat 2 (HR2) (*19*, *20*). These large structural rearrangements bring together the viral and cellular membranes, ultimately leading to fusion of the two bilayers.

Since the first genome sequence of SARS-CoV-2 was released (*21*), several structures have been reported for S protein complexes, including the ectodomain stabilized in the prefusion conformation (*22*–*24*) and RBD-ACE2 complexes (*25*–*28*) (fig. S1), building upon the previous success of the structural biology of S proteins from other CoVs (*20*). In the stabilized S ectodomain, S1 folds into four domains, the N-terminal domain (NTD), RBD, and two C-terminal domains (CTDs), and protects the prefusion conformation of S2, in which HR1 bends back toward the viral membrane (fig. S1, A and B). The RBD samples two distinct conformations, with "up" representing a receptor-accessible state and "down" representing a receptor-inaccessible state. Structures representing the postfusion state of S2 from mouse hepatitis virus (MHV) (fig. S1E) and the one at a lower resolution from SARS-CoV (fig. S1F) suggest how the structural rearrangements of S2 proceed to promote membrane fusion and viral entry (*29*, *30*). Comparison of the pre- and postfusion states reveals that HR1 undergoes a "jackknife" transition that can insert the fusion peptide (FP) into the target cell membrane. Folding back of HR2 places the FP and transmembrane (TM) segments at the same end of the molecule, causing the membranes with which they interact to bend toward each other, effectively leading to membrane fusion. In the previous structures, the regions near the viral membrane were either not present or disordered, yet they all appeared to play critical structural and functional roles (*31*–*35*).

To gain further insight, we aimed to determine the pre- and postfusion states of the full-length wild-type S protein of SARS-CoV-2.

Results

Purification of intact S protein

To produce a functional SARS-CoV-2 S protein, we transfected human embryonic kidney (HEK) 293 cells with an expression construct of a full-length wild-type S sequence with a C-terminal Strep-tag (Fig. 1A). These cells fused efficiently with cells transfected with an intact human ACE2 construct even without the addition of any extra proteases (fig. S2), suggesting that the S protein expressed on the cell surfaces is fully functional for membrane fusion. The fusion efficiency was not affected by the C-terminal Strep-tag. To purify the full-length S protein, we lysed the cells and solubilized all membrane-bound proteins in 1% NP-40 detergent. The Strep-tagged S protein was then captured on Strep-tactin resin in 0.3% NP-40. The purified S protein eluted from a size-exclusion column as three distinct peaks in 0.02% NP-40 (Fig. 1B). Analysis by Coomassie blue–stained sodium dodecyl sulfate–polyacrylamide gel electrophoresis (SDS-PAGE) (Fig. 1C) showed that peak 1 contained both the uncleaved S precursor and the cleaved S1/S2 complex; peak 2 had primarily the cleaved but dissociated S2 fragment; and peak 3 included mainly the dissociated S1 fragment, as judged by N-terminal sequencing and Western blot (fig. S3). This was confirmed by negative-stain electron microscopy (EM) (Fig. 1C). Peak 1 showed the strongest binding to soluble ACE2, comparable to that for the purified soluble S ectodomain trimer, and peak 2 showed the weakest binding because it contained mainly the S2 fragment (fig. S4). Although cleavage

[1]Division of Molecular Medicine, Boston Children's Hospital, Boston, MA 02115, USA. [2]Department of Pediatrics, Harvard Medical School, Boston, MA 02115, USA. [3]The Harvard Cryo-EM Center for Structural Biology, Harvard Medical School, Boston, MA 02115, USA. [4]Department of Biological Chemistry and Molecular Pharmacology, Blavatnik Institute, Harvard Medical School, Boston, MA 02115, USA. [5]SBGrid Consortium, Harvard Medical School, Boston, MA 02115, USA.
*These authors contributed equally to this work.
†Corresponding author. Email: bchen@crystal.harvard.edu

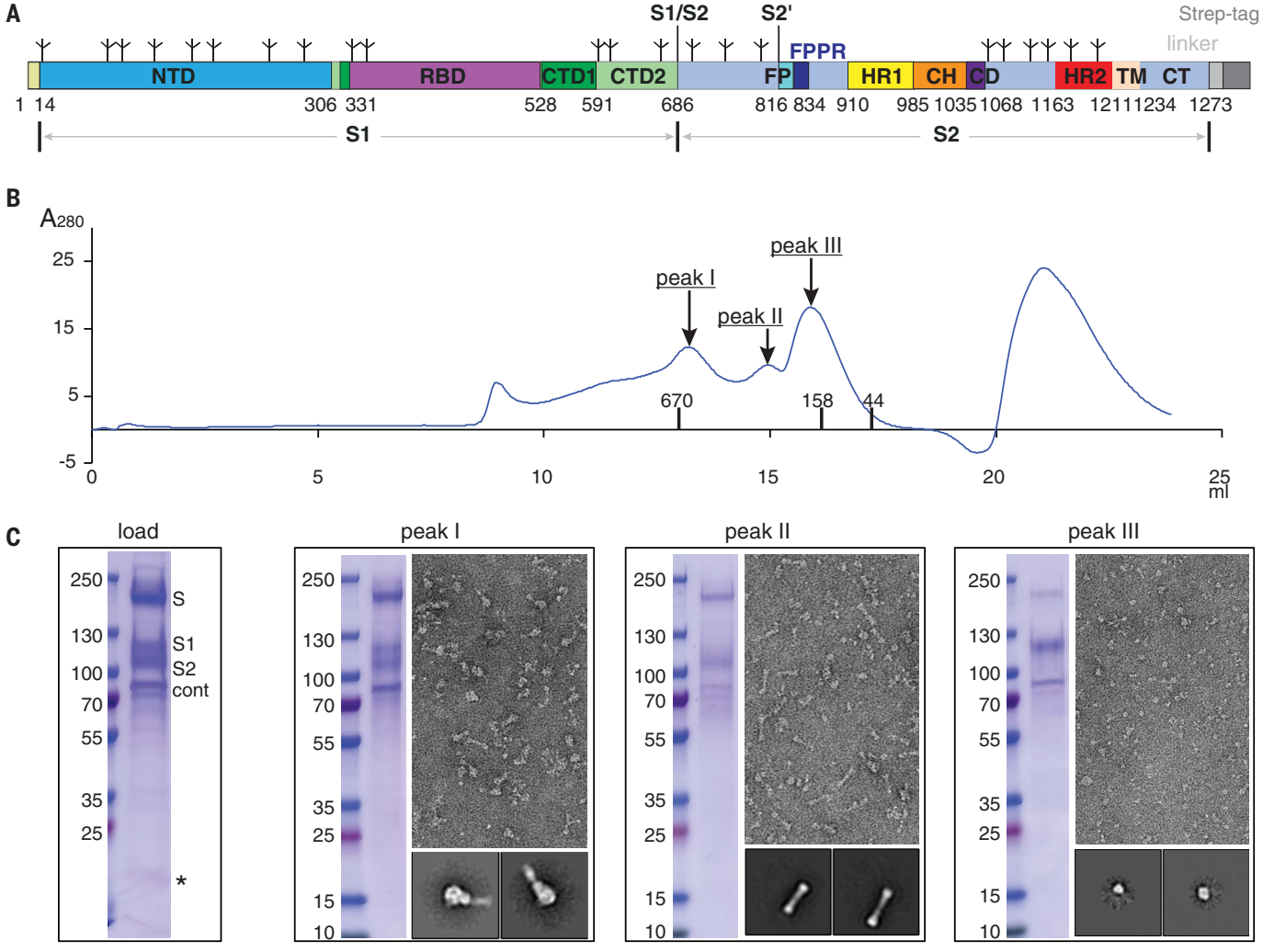

Fig. 1. Preparation of a full-length SARS-CoV-2 spike protein. (**A**) Schematic representation of the expression construct of full-length SARS-CoV-2 S protein. Segments of S1 and S2 include NTD, RBD, CTD1, CTD2, S1/S2, S2', FP, FPPR, HR1, CH, CD, HR2, TM, CT, and tree-like symbols for glycans. A Strep-tag was fused to the C terminus of S protein by a flexible linker. (**B**) The purified S protein was resolved by gel-filtration chromatography on a Superose 6 column in the presence of NP-40. The molecular weight standards include thyoglobulin (670 kDa), γ-globulin (158 kDa), and ovalbumin (44 kDa). Three major peaks (peaks I, II, and III) contain the S protein. (**C**) Load sample and peak fractions from (B) were analyzed by Coomassie blue–stained SDS-PAGE. Labeled bands were confirmed by Western blot (S, S1, and S2) or protein sequencing (S2 and Cont; S and S1 bands did not gave any meaningful results, probably because of a blocked N terminus). Cont, copurified contaminating protein, identified as endoplasmic reticulum chaperone BiP precursor by N-terminal sequencing. *Putative S1/S2-S2' fragment. Representative images and 2D averages by negative-stain EM of three peak fractions are also shown. The box size of 2D averages is ~510 Å.

at the S1/S2 (furin) site was clearly demonstrated by protein sequencing of the N terminus of the S2 fragment in peak 2, cleavage at the S2' site was not obvious. In some preparations, we observed a band around 20 kDa, a size expected for the S1/S2-S2' fragment (Fig. 1C). We obtained a similar gel filtration profile when another detergent (dodecyl maltoside) was used to solubilize the S protein (fig. S5), suggesting that the S protein dissociation during gel filtration chromatography is not triggered by any specific detergent. We also identified a major contaminating protein in the preparation as endoplasmic reticulum chaperone binding protein (BiP) precursor (*36*), which may have a role in facilitating S protein folding.

Cryo-EM structure determination

Cryo-EM images were acquired with selected grids prepared from all three peaks on a Titan Krios electron microscope operated at 300 keV and equipped with a BioQuantum energy filter and a Gatan K3 direct electron detector. RELION (*37*) was used for particle picking, two-dimensional (2D) classification, 3D classification, and refinement. Structure determination was performed by rounds of 3D classification, refinement, and masked local refinement, as described in the supplementary materials. The final resolution was 2.9 Å for the prefusion S protein and 3.0 Å for S2 in the postfusion conformation (figs. S6 to S9).

Structure of the prefusion S trimer

The overall architecture of the full-length S protein in the prefusion conformation was very similar to the published structures of a soluble S trimer stabilized by a C-terminal foldon trimerization tag and two proline substitutions at the boundary between HR1 and the central helix (CH) in S2 (fig. S1) (*22*, *23*). In our new structure, the N terminus, several peripheral loops, and glycans that were invisible in the soluble trimer structures are ordered (Fig. 2, A and B, and fig. S10A). As described previously, the four domains of the S1 fragment, NTD, RBD, CTD1, and CTD2, wrap around the threefold axis, covering the S2 fragment underneath. The furin cleavage

site at the S1/S2 boundary is in a surface-exposed and disordered loop (Fig. 2B), so it is unclear whether this structure represents the uncleaved or cleaved trimer, although the sample clearly contains both forms (Fig. 1C). Likewise, the S2 fragment has a conformation nearly identical to that in the previous trimer structures, with most of the polypeptide chain packed around a central three-stranded coiled coil formed by CH, including the connector domain (CD), which links CH and the C-terminal HR2 through an additional linker region. A difference between our structure and the published trimer structures is that an ~25-residue segment in S2 immediately downstream of the fusion peptide is ordered. The segments HR2, TM, and CT, which were not observed in previous structures, are still not visible.

Several features are different between our structure and the previously described prefusion

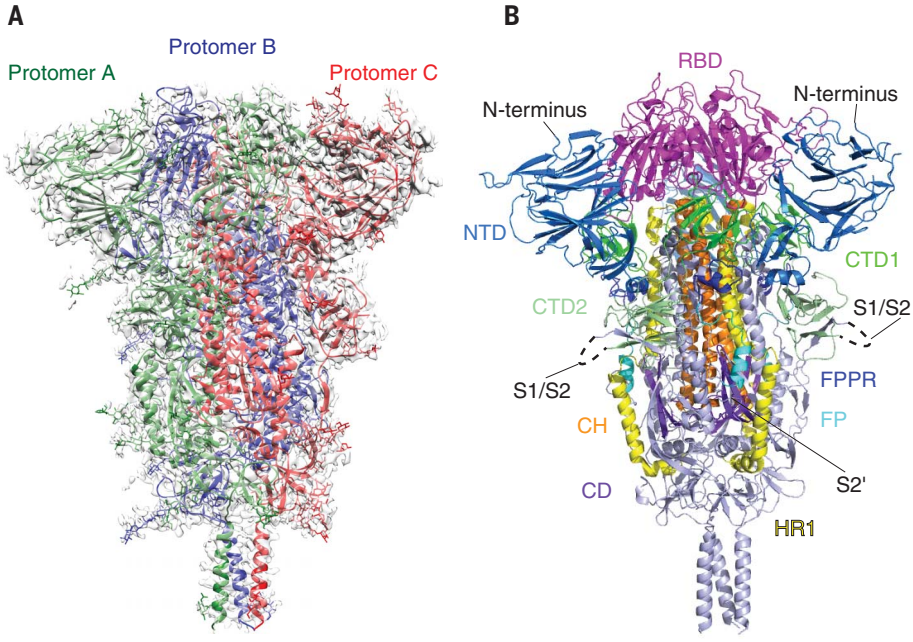

Fig. 2. Cryo-EM structure of the SARS-CoV-2 S protein in the prefusion conformation. (**A**) The structure of the S trimer was modeled based on a 2.9-Å density map. Three protomers (A, B, and C) are colored in green, blue, and red, respectively. (**B**) Overall structure of S protein in the prefusion conformation shown in ribbon representation. Various structural components in the color scheme shown in Fig. 1A include NTD, RBD, CTD1, CTD2, FP, FPPR, HR1, CH, and CD. The N terminus, S1/S2 cleavage site, and S2' cleavage site are indicated.

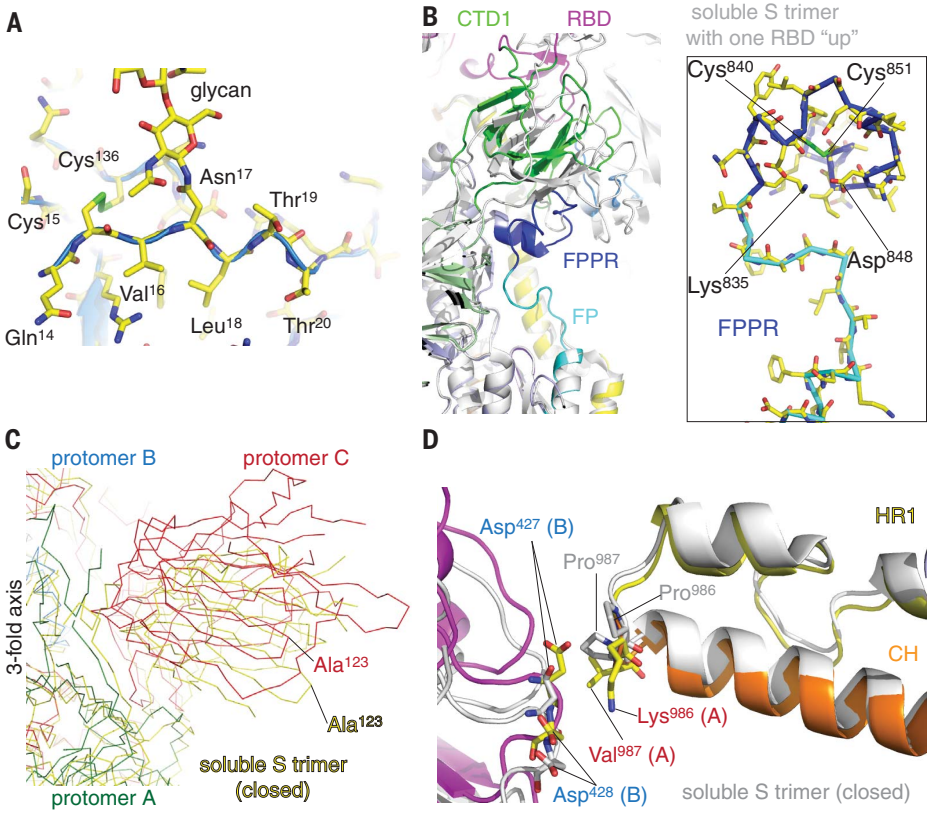

Fig. 3. Selected new features of the SARS-CoV-2 prefusion S trimer. (**A**) N-terminal segment of the S protein. The N terminus is at residue Gln^{14} after cleavage of the signal peptide. Cys^{15} forms a disulfide bond with Cys^{136}. We observed good density for the N-linked glycan at Asn^{17}. (**B**) A segment immediately downstream of the fusion peptide, designated FPPR, although disordered in the stabilized soluble S ectodomain trimer structure, forms a tightly packed structure, abutting CTD1. The newly identified FPPR structure would clash with CTD1 in the RBD up conformation. Various domains are shown in the color scheme in Fig. 2B. The structure of the soluble S trimer with one RBD in the up conformation (PDB ID: 6vyb) is shown in gray. Box shows a close-up view of the FPPR with the adjacent fusion peptide in both a surface representation and a stick model. (**C**) The SARS-CoV-2 prefusion S trimer, viewed along the threefold axis, is superposed on the structure of the stabilized soluble S ectodomain trimer in the closed conformation with all three RBDs in the down conformation (PDB ID: 6vxx). Although the S2 region is well aligned, there is a significant shift (e.g., ~12 Å between two Ala^{123} residues) in S1. (**D**) Impact of the proline mutations introduced at residues 986 and 987 to stabilize the prefusion conformation. K986P mutation removes a salt bridge between Lys^{986} of one protomer and either Asp^{427} or Asp^{428} of another protomer in the trimer interface.

conformations. First, the N terminus in our structure is ordered and adopts a conformation similar to that in SARS-CoV, including a disulfide bond (Cys^{15}–Cys^{136}) and an N-linked glycan at Asn^{17} (Fig. 3A) (*38*). It will be important to confirm whether this region is unfolded with no disulfide bond in the stabilized soluble constructs or if it is folded and simply poorly defined by density despite a disulfide bond, particularly if these constructs are widely used for vaccine studies.

Second, another disulfide-containing segment (residues 828 to 853) immediately downstream of the fusion peptide is also absent from the structures of the soluble ectodomain but ordered in our structure (Fig. 3B). We designate it as the fusion-peptide proximal region (FPPR). The FPPR is disordered in both the closed and RBD-up conformations of the stabilized soluble S trimer. In our full-length structure, it packs rather tightly around an internal disulfide bond between Cys^{840} and Cys^{851}, further reinforced by a salt bridge between Lys^{835} and Asp^{848}, as well as by an extensive hydrogen bond network. When compared with the RBD-up conformation by superposition of the rest of S2, the FPPR clashes with CTD1, which rotates outward with the RBD in the flipping-up transition. Thus, a structured FPPR abutting the opposite side of CTD1 from the RBD appears to help clamp down the RBD and stabilize the closed conformation of the S trimer. It is not obvious why the FPPR is also not visible in the published, closed S ectodomain structure with all three RBDs in the down conformation (*23*). Our structure of the full-length S protein suggests that CTD1 is a structural relay between RBD and FPPR that can sense the displacement on either side. The latter is directly connected to the fusion peptide. Lack of a structured FPPR in the stabilized, soluble S trimer may explain why the RBD-up conformation is readily detected in that preparation. In addition, a D614G mutation that was identified in recent SARS-CoV-2 isolates has been suggested to lead to more efficient entry (*39*, *40*). D614 forms a salt bridge with K854 in the FPPR (fig. S10B), supporting a functional role of the FPPR in membrane fusion. In the 3D classification of our prefusion particles from two independent datasets, only one subclass with an RBD flipped up was observed (fig. S6), suggesting that the RBD-up conformation is relatively rare in our full-length S preparation. The map for this subclass was refined to 4.7 Å without C3 symmetry, and we could not model the FPPR. The FPPR is ordered in all other maps that are refined to 3.5 Å or higher resolution.

When we aligned our full-length structure with the soluble S trimer structure by the S2 portion, the three S1 subunits in the soluble trimer structure moved outward, away from the threefold axis, up to ~12 Å in peripheral areas (Fig. 3C and fig. S11), suggesting that the full-length S trimer is more tightly packed among the three protomers than the mutated soluble trimer. Examining the region near the proline mutations between HR1 and CH, we found that the K986P mutation appeared to eliminate a salt bridge between Lys^{986} in one protomer and either Asp^{427} or Asp^{428} in another protomer; thus, the mutation could create a net charge (three for one trimer) inside the trimer interface. This may explain why the soluble trimer with the PP mutation has a looser structure than the full-length S with the wild-type sequence. Whether this loosening leads to disordered FPPRs in the closed trimer will require additional experimental evidence. However, the proline mutations, designed to destabilize the postfusion conformation and strengthen the prefusion structure, may also affect the prefusion structure.

Structure of the postfusion S2 trimer

Three-dimensional reconstruction of the sample from peak 2 yielded a postfusion structure of the S2 trimer, shown in Fig. 4A. The overall architecture of the SARS-CoV-2 S2 in the postfusion conformation is nearly identical to that of the published structure derived from the S2 ectodomain of MHV produced in insect cells (fig. S1) (*29*). In the structure, HR1 and CH form an unusually long, central, three-stranded coiled coil (~180 Å). The connector domain, together with a segment (residues 718 to 729) in the S1/S2-S2' fragment, form a three-stranded β sheet, which is invariant between the prefusion and postfusion structures. In the postfusion state, residues 1127 to 1135 join the connector β sheet to expand it into four strands while projecting the C-terminal HR2 toward the viral membrane. Another segment (residues 737 to 769) in the S1/S2-S2' fragment makes up three helical regions locked by two disulfide bonds that pack against the groove of the CH part of the coiled coil to form a short, six-helix bundle structure (6HB-1 in Fig. 4B). It is unclear whether the S2' site is cleaved because it is in a disordered region spanning 142 residues (Fig. 4B), as in the MHV S2 structure. Nevertheless, the S1/S2-S2' fragment is an integral part of the postfusion structure and would not dissociate regardless of cleavage at the S2' site. The N-terminal region of HR2 adopts a one-turn helical conformation and also packs against the groove of the HR1 coiled coil; the C-terminal region of HR2 forms a longer helix that makes up the second six-helix bundle structure with the rest of the HR1 coiled coil (6HB-2 in Fig. 4B). Thus, the long central coiled coil is reinforced multiple times along its long axis, making it a very rigid structure, as evident even from 2D class averages of particles in the cryo-EM images (fig. S8).

A striking feature of the postfusion S2 is its surface decoration by N-linked glycans (Fig. 4C),

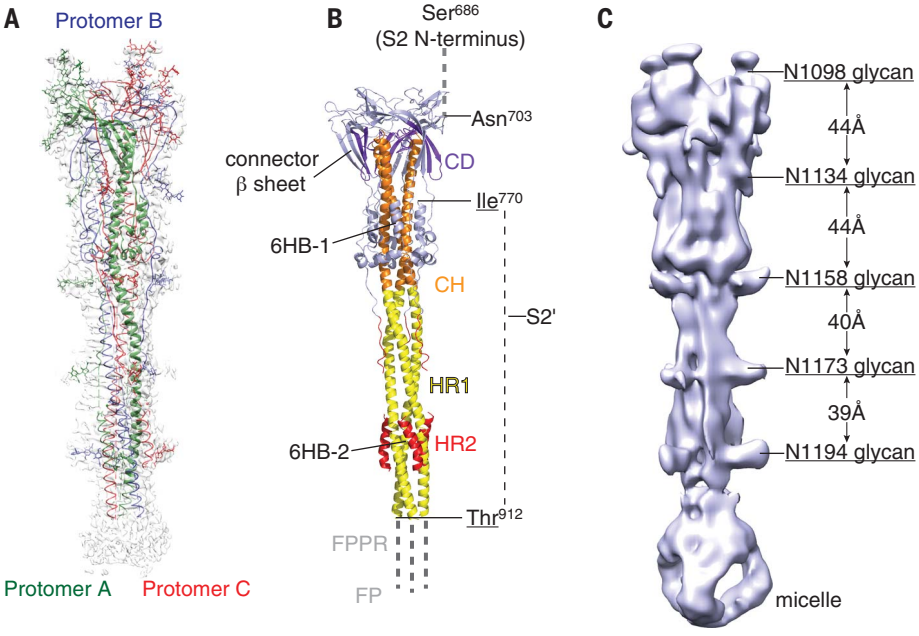

Fig. 4. Cryo-EM structure of the SARS-CoV-2 S2 in the postfusion conformation. (**A**) The structure of the S2 trimer was modeled based on a 3.0-Å density map. Three protomers (A, B, and C) are colored in green, blue, and red, respectively. (**B**) Overall structure of the S2 trimer in the postfusion conformation shown in ribbon diagram. Various structural components in the color scheme shown in Fig. 1A include HR1, CH, CD, and HR1. The S2' cleavage site is in a disordered loop between Ile^{770} and Thr^{912}. Possible locations of the S2 N terminus (S1/S2 cleavage site), FP, and FPPR are also indicated. (**C**) Low-resolution map showing the density pattern for five N-linked glycans, with almost equal spacing along the long axis.

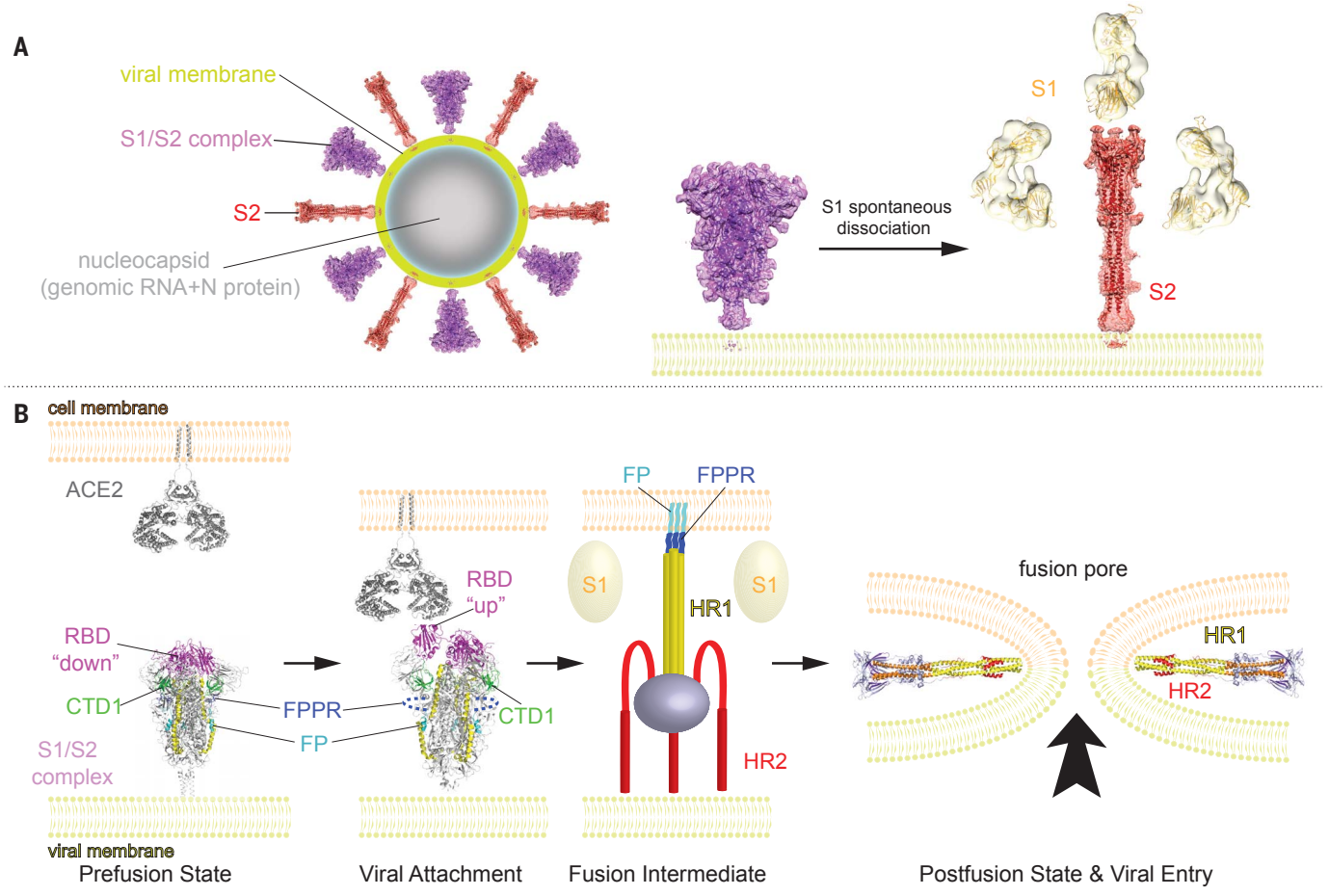

Fig. 5. Model for structural rearrangements of SARS-Cov-2 S protein. (**A**) Structural changes independent of a target cell. We suggest that both the prefusion and postfusion spikes are present on the surface of mature virion and the ratio between them may vary. A diagram of the virion is shown. The postfusion spikes on the virion are formed by S2 after S1 dissociates in the absence of ACE2. (**B**) ACE2-dependent structural rearrangements. Structural transition from the prefusion to postfusion conformation inducing membrane fusion likely proceeds stepwise as follows. First, FPPR clamps down RBD through CTD1 in the prefusion S trimer (this study) but occasionally flips out of position and allows an RBD to sample the up conformation (PDB ID: 6vyb). Second, RBD binding to ACE2 (PDB ID: 6m17) creates a flexible FPPR that enables exposure of the S2' cleavage site immediately upstream of the adjacent FP. Cleavage at the S2' site, and perhaps also the S1/S2 site, releases the structural constraints on the fusion peptide and initiates a cascade of refolding events in S2, probably accompanied by complete dissociation of S1. Third, the long, central, three-stranded coiled coil forms and HR2 folds back. Finally, the postfusion structure of S2 (this study) forms, which brings the two membranes together, facilitating formation of a fusion pore and viral entry.

also visible in the 2D class averages (fig. S8). Five glycans at residues Asn^{1098}, Asn^{1134}, Asn^{1158}, Asn^{1173}, and Asn^{1194} are positioned along the long axis with a regular spacing and four of them aligned on the same side of the trimer. If these glycosylation sites are fully occupied by branched sugars, then they may shield most surfaces of the postfusion S2 trimer. A similar pattern has been described recently (*41*) for a SARS-CoV S2 preparation derived from a soluble S ectodomain construct produced in insect cells and triggered by proteolysis and low pH. The reason for this decoration is unclear given that a postfusion structure has accomplished its mission and should not need to be concealed from the immune system.

Peak 3 contains primarily the dissociated monomeric S1 fragment, which is the smallest (~100 kDa) and shows the lowest contrast in cryo-EM grids of the three particle types we describe. We performed a preliminary 3D reconstruction analysis (fig. S12), further confirming its identity.

Discussion

Architecture of S protein on the surface of SARS-CoV-2 virion

The fact that the cleaved S1/S2 complex dissociates in the absence of ACE2 and that the S2 fragment adopts a postfusion conformation under mild detergent conditions suggests that the kinetic barrier for the conformational transition relevant to viral entry is surprisingly low for this S protein. Whether this observation relates directly to efficient membrane fusion or infection is unclear. Nevertheless, it is noteworthy that the postfusion S2 trimer not only has a very stable and rigid structure, but is also strategically decorated with N-linked glycans along its long axis as if under selective pressure for functions other than the membrane fusion process. Although some have suggested that viral fusion proteins may further oligomerize in their postfusion conformation to facilitate fusion pore formation (*42*), the protruding surface glycans of the SARS-CoV-2 S2 make this scenario unlikely. A more plausible possibility is a protective role that the S2 postfusion structure could play if it is also present on the surface of an infectious and mature virion. It may induce non-neutralizing antibody responses to evade the host immune system, and it may also shield the more vulnerable prefusion S1/S2 trimers under conditions outside the host by decorating the viral surface with interspersed rigid spikes (Fig. 5A). Several recent reports have provided some evidence

supporting this possibility. First, EM images of a β-propiolactone–inactivated SARS-CoV-2 virus preparation purified by a potassium tartrate–glycerol density gradient appeared to have lost all S1 subunits, leaving only the postfusion S2 on the virion surfaces (*43*). Likewise, EM images of a β-propiolactone–inactivated SARS-CoV-2 virus vaccine candidate (PiCoVacc) also showed needle-like spikes on its surfaces (*44*). Second, spontaneous shedding of SARS-CoV-2 S1 from pseudoviruses in the absence of ACE2 has been reported (*39*). Third, binding antibodies against S2 are readily detectable in COVID-19 patients (*45*), suggesting that S2 is more exposed to the host immune system than indicated by the unprotected surfaces on the prefusion structures (*22*, *23*) (Fig. 2). We therefore suggest that postfusion S2 trimers may have a protective function by constituting part of the crown on the surface of mature and infectious SARS-CoV-2 virion (Fig. 5). The postfusion S2 spikes are probably formed after spontaneous dissociation of S1 independently of the target cells.

Membrane fusion

We identify a structure near the fusion peptide, the FPPR, that may play a critical role in the fusogenic structural rearrangements of the S protein. There appears to be cross-talk between the RBD and the FPPR, mediated by CTD1, because a structured FPPR clamps down the RBD whereas an RBD-up conformation disorders the FPPR. Moreover, the FPPR is close to the S1/S2 boundary and the S2' cleavage site and thus might be the center of activities relevant to conformational changes in S. One possibility is that one FPPR occasionally flips out of position due to intrinsic protein dynamics, allowing the RBDs to sample the up conformation. A fluctuation of this kind would loosen the entire S trimer, as observed in modified soluble S trimer constructs (*22*, *23*). Once an RBD is fixed in the up position by binding to ACE2 on the surface of a target cell, a flexible FPPR may enable exposure of the S2' cleavage site immediately upstream of the adjacent fusion peptide. The phenotype of the D614G mutation appears to be consistent with the notion that the FPPR is involved in membrane fusion (*39*, *40*). Cleavage at the S2' site releases the structural constraints on the fusion peptide, which may initiate a cascade of refolding events in S2, including formation of the long, central, three-stranded coiled coil; folding back of HR2; and ultimately membrane fusion. Cleavage at the S1/S2 site allows complete dissociation of S1, which may also facilitate S2 refolding.

Questions regarding membrane fusion remain because the regions near the viral membrane are still not visible in the reconstructions. However, these regions all play critical structural and functional roles. For example, the conserved hydrophobic region immediately preceding the TM domain, and possibly the TM itself, have been shown to be crucial for S protein trimerization and membrane fusion (*31*). The cytoplasmic tail, containing a palmitoylated, cysteine-rich region, is believed to be involved in viral assembly and cell-cell fusion (*32*–*35*). Whether other viral proteins, such as M protein, may help to stabilize the spike by interacting with HR2 remains an open question. Thus, we still need a high-resolution structure of an intact S protein in the context of the membrane and other viral components to answer such questions.

Considerations for vaccine development

A safe and effective vaccine is the primary medical option to reduce or eliminate the threat posed by SARS-CoV-2. The first round of vaccine candidates with various forms of the S protein of the virus are passing rapidly through preclinical studies in animal models and clinical trials in humans. Our study raises several potential concerns about the current vaccine strategies. First, vaccines using the full-length wild-type sequence of the S protein may produce the various forms in vivo that we have observed here. The postfusion conformations could expose immunodominant, non-neutralizing epitopes that distract the host immune system, as documented for other viruses such as HIV-1 and RSV (*46*, *47*). Second, the approach to stabilizing the prefusion conformation by introducing proline mutations at residues 986 and 987 may not be optimal because the K986P mutation may break a salt bridge between protomers that contributes to trimer stability. The resulting S trimer structure with a relaxed apex may induce antibodies that could not efficiently recognize S trimer spikes on the virus, although it may be more effective in inducing anti-RBD–neutralizing responses than the closed form. Third, considering the possibility that the postfusion S2 is present on infectious virions, vaccines using β-propiolactone–inactivated viruses may require additional quality control tests. Although the PiCoVacc appears to provide protection against challenges in nonhuman primates after three immunizations (*44*), it is unclear how to minimize the number of the postfusion S2 trimers to avoid batch variations. Structure-guided immunogen design may be particularly critical if SARS-CoV-2 becomes seasonal and returns with antigenic drift, as do influenza viruses (*48*).

REFERENCES AND NOTES

1. E. de Wit, N. van Doremalen, D. Falzarano, V. J. Munster, *Nat. Rev. Microbiol.* **14**, 523–534 (2016).
2. N. S. Zhong *et al.*, *Lancet* **362**, 1353–1358 (2003).
3. B. Hijawi *et al.*, *East. Mediterr. Health J.* **19**, S12–S18 (2013).
4. V. M. Corman, D. Muth, D. Niemeyer, C. Drosten, *Adv. Virus Res.* **100**, 163–188 (2018).
5. Y. Guan *et al.*, *Science* **302**, 276–278 (2003).
6. B. Hu *et al.*, *PLOS Pathog.* **13**, e1006698 (2017).
7. H. A. Mohd, J. A. Al-Tawfiq, Z. A. Memish, *Virol. J.* **13**, 87 (2016).
8. A. Banerjee, K. Kulcsar, V. Misra, M. Frieman, K. Mossman, *Viruses* **11**, 41 (2019).
9. P. Zhou *et al.*, *Nature* **579**, 270–273 (2020).
10. S. Belouzard, J. K. Millet, B. N. Licitra, G. R. Whittaker, *Viruses* **4**, 1011–1033 (2012).
11. R. P. Rand, V. A. Parsegian, *Can. J. Biochem. Cell Biol.* **62**, 752–759 (1984).
12. V. A. Parsegian, N. Fuller, R. P. Rand, *Proc. Natl. Acad. Sci. U.S.A.* **76**, 2750–2754 (1979).
13. S. C. Harrison, *Virology* **479-480**, 498–507 (2015).
14. M. Kielian, *Annu. Rev. Virol.* **1**, 171–189 (2014).
15. W. Weissenhorn *et al.*, *Mol. Membr. Biol.* **16**, 3–9 (1999).
16. L. Du *et al.*, *Nat. Rev. Microbiol.* **7**, 226–236 (2009).
17. B. J. Bosch, R. van der Zee, C. A. de Haan, P. J. Rottier, *J. Virol.* **77**, 8801–8811 (2003).
18. M. Hoffmann *et al.*, *Cell* **181**, 271–280.e8 (2020).
19. J. K. Millet, G. R. Whittaker, *Proc. Natl. Acad. Sci. U.S.A.* **111**, 15214–15219 (2014).
20. M. A. Tortorici, D. Veesler, *Adv. Virus Res.* **105**, 93–116 (2019).
21. F. Wu *et al.*, *Nature* **579**, 265–269 (2020).
22. D. Wrapp *et al.*, *Science* **367**, 1260–1263 (2020).
23. A. C. Walls *et al.*, *Cell* **181**, 281–292.e6 (2020).
24. R. Henderson *et al.*, bioRxiv 2020.05.18.102087 [Preprint]. 18 May 2020. https://doi.org/10.1101/2020.05.18.102087.
25. J. Lan *et al.*, *Nature* **581**, 215–220 (2020).
26. R. Yan *et al.*, *Science* **367**, 1444–1448 (2020).
27. J. Shang *et al.*, *Nature* **581**, 221–224 (2020).
28. Q. Wang *et al.*, *Cell* **181**, 894–904.e9 (2020).
29. A. C. Walls *et al.*, *Proc. Natl. Acad. Sci. U.S.A.* **114**, 11157–11162 (2017).
30. W. Song, M. Gui, X. Wang, Y. Xiang, *PLOS Pathog.* **14**, e1007236 (2018).
31. B. Schroth-Diez *et al.*, *Biosci. Rep.* **20**, 571–595 (2000).
32. B. J. Bosch, C. A. de Haan, S. L. Smits, P. J. Rottier, *Virology* **334**, 306–318 (2005).
33. E. Lontok, E. Corse, C. E. Machamer, *J. Virol.* **78**, 5913–5922 (2004).
34. C. M. Petit *et al.*, *Virology* **341**, 215–230 (2005).
35. R. Ye, C. Montalto-Morrison, P. S. Masters, *J. Virol.* **78**, 9904–9917 (2004).
36. S. M. Hurtley, D. G. Bole, H. Hoover-Litty, A. Helenius, C. S. Copeland, *J. Cell Biol.* **108**, 2117–2126 (1989).
37. S. H. Scheres, *J. Struct. Biol.* **180**, 519–530 (2012).
38. R. N. Kirchdoerfer *et al.*, *Sci. Rep.* **8**, 15701 (2018).
39. L. Zhang *et al.*, bioRxiv 2020.06.12.148726 [Preprint]. 12 June 2020. https://doi.org/10.1101/2020.06.12.148726.
40. Z. Daniloski *et al.*, bioRxiv 10.1101/2020.06.14.151357 [Preprint]. 7 July 2020. https://doi.org/10.1101/2020.06.14.151357.
41. X. Fan, D. Cao, L. Kong, X. Zhang, *Nat. Commun.* **11**, 3618 (2020).
42. T. Danieli, S. L. Pelletier, Y. I. Henis, J. M. White, *J. Cell Biol.* **133**, 559–569 (1996).
43. C. Liu *et al.*, bioRxiv 2020.03.02.972927 [Preprint]. 5 March 2020. https://doi.org/10.1101/2020.03.02.972927.
44. Q. Gao *et al.*, *Science* **369**, 77–81 (2020).
45. F. Wu *et al.*, medRxiv 2020.03.30.20047365 [Preprint]. 20 April 2020. https://doi.org/10.1101/2020.03.30.20047365.
46. J. S. McLellan *et al.*, *Science* **342**, 592–598 (2013).
47. G. Frey *et al.*, *Nat. Struct. Mol. Biol.* **17**, 1486–1491 (2010).
48. J. J. Skehel, D. C. Wiley, *Annu. Rev. Biochem.* **69**, 531–569 (2000).

ACKNOWLEDGMENTS

We thank M. Liao for generous advice; the SBGrid team for technical support; and S. Harrison, M. Liao, A. Carfi, and D. Barouch for critical reading of the manuscript. Negative-stain and cryo-EM data were collected at the Molecular Electron Microscopy Suite and the Harvard Cryo-EM Center for Structural Biology, respectively, at Harvard Medical School. **Funding:** This work was supported by NIH grants AI147884 (to B.C.), 3R01AI147884-01A1S1 (to B.C), AI141002 (to B.C.), and AI127193 (to B.C. and James Chou), as well as a COVID-19 Award by Massachusetts Consortium on Pathogen Readiness (MassCPR; to B.C.). **Author contributions:** B.C. and Y.C. conceived the project. Y.C. and H.P. expressed and purified the full-length S protein. T.X. expressed and purified soluble ACE2 and performed SPR and cell-cell fusion experiments. Y.C. and J.Z. performed negative-stain EM analysis. J.Z. prepared cryo-EM grids and performed EM data collection with contributions from S.M.S. and R.M.W. J.Z. processed the cryo-EM data and built and refined the atomic models for the prefusion S trimer and the postfusion S2 trimer. Y.C. processed the S1 data. S.R. contributed to data processing for S1 and provided computational support. S.R.-V. contributed to cell culture and protein production. All authors analyzed the data. B.C., Y.C., J.Z., and T.X. wrote the manuscript with input from all other authors. **Competing interests:** The authors

declare no competing interests. **Data and materials availability:** The atomic structure coordinates have been deposited in the RCSB Protein Data Bank (PDB) under the accession numbers 6XR8 and 6XRA, and the electron microscopy maps have been deposited in the Electron Microscopy Data Bank (EMDB) under the accession numbers EMD-22292 and EMD-22293. All materials generated during the current study are available from the corresponding author under a materials transfer agreement with Boston Children's Hospital.

SUPPLEMENTARY MATERIALS

science.sciencemag.org/content/369/6511/1586/suppl/DC1
Materials and Methods
Figs. S1 to S12
Table S1
References (*49*–*58*)
MDAR Reproducibility Checklist

View/request a protocol for this paper from *Bio-protocol*.

20 June 2020; accepted 14 July 2020
Published online 21 July 2020
10.1126/science.abd4251

Science

Distinct conformational states of SARS-CoV-2 spike protein

Yongfei Cai, Jun Zhang, Tianshu Xiao, Hanqin Peng, Sarah M. Sterling, Richard M. Walsh Jr., Shaun Rawson, Sophia Rits-Volloch and Bing Chen

Science **369** (6511), 1586-1592.
DOI: 10.1126/science.abd4251originally published online July 21, 2020

A dynamic viral spike

Efforts to protect human cells against severe acute respiratory syndrome coronavirus 2 (SARS-CoV-2) have focused on the trimeric spike (S) protein. Several structures have shown a stabilized ectodomain of the spike in its prefusion conformation. Cai *et al.* now provide insight into the structural changes in the S protein that result in the fusion of the viral and host cell membranes. They purified full-length S protein and determined cryo–electron microscopy structures of both the prefusion and postfusion conformations. These structures add to our understanding of S protein function and could inform vaccine design.

Science, this issue p. 1586

Science (print ISSN 0036-8075; online ISSN 1095-9203) is published by the American Association for the Advancement of Science, 1200 New York Avenue NW, Washington, DC 20005. The title *Science* is a registered trademark of AAAS.